

Pose Modulated Avatars from Video

Chunjin Song¹, Bastian Wandt², Helge Rhodin¹

¹University of British Columbia

²Linköping University

Abstract

It is now possible to reconstruct dynamic human motion and shape from a sparse set of cameras using Neural Radiance Fields (NeRF) driven by an underlying skeleton. However, a challenge remains to model the deformation of cloth and skin in relation to skeleton pose. Unlike existing avatar models that are learned implicitly or rely on a proxy surface, our approach is motivated by the observation that different poses necessitate unique frequency assignments. Neglecting this distinction yields noisy artifacts in smooth areas or blurs fine-grained texture and shape details in sharp regions. We develop a two-branch neural network that is adaptive and explicit in the frequency domain. The first branch is a graph neural network that models correlations among body parts locally, taking skeleton pose as input. The second branch combines these correlation features to a set of global frequencies and then modulates the feature encoding. Our experiments demonstrate that our network outperforms state-of-the-art methods in terms of preserving details and generalization capabilities.

Introduction

Human avatar modeling has garnered significant attention as enabling 3D telepresence and digitization with applications ranging from computer graphics (Bagautdinov et al. 2021; Peng et al. 2021a; Lombardi et al. 2021) to medical diagnosis (Hu et al. 2022). To tackle this challenge, the majority of approaches start from a skeleton structure that rigs a surface mesh equipped with a neural texture (Bagautdinov et al. 2021; Liu et al. 2021) or learnable vertex features (Kwon et al. 2021; Peng et al. 2021a,b). Although this enables reconstructing intricate details with high precision (Liu et al. 2021; Thies, Zollhöfer, and Nießner 2019) in controlled conditions, artifacts remain when learning the pose-dependent deformation from sparse examples. To counteract, existing methods typically rely on a parametric template obtained from a large number of laser scans, which still limits the variety of the human shape and pose. Moreover, their explicit notion of vertices and faces is difficult to optimize and can easily lead to foldovers and artifacts from other degenerate configurations. Moreover, the processed meshes are usually

sampled uniformly in one static pose thus not being adaptive to dynamic shape details like wrinkles.

Our objective is to directly reconstruct human models with intricate and dynamic details from given video sequences with a learned neural radiance field (NeRF) model (Mildenhall et al. 2020). Most related are surface-free approaches such as A-NeRF (Su et al. 2021) and NARF (Noguchi et al. 2021) that directly transform the input query points into relative coordinates of skeletal joints and then predict density and color for volumetric rendering without an intermediate surface representation. To further enhance the ability to synthesize fine details, (Su, Bagautdinov, and Rhodin 2022; Li et al. 2023) explicitly decompose features into local part encodings before aggregating them to the final color. Closely related are also methods that learn a neural radiance field of the person in a canonical T-pose (Jiang et al. 2022; Li et al. 2022a; Wang et al. 2022). Despite their empirical success, as depicted in Fig. 1, it is evident that a single query point, when considered in different pose contexts, is difficult to be learned. Specifically, the T-shirt region appears flat in one pose (2nd row) but transforms into a highly textured surface in another (1st row). The commonly used positional encoding (Mildenhall et al. 2020) maps points with fixed frequency transformations and is hence non-adaptive. Entirely implicit mappings from observation to canonical space are complex and contain ill-posed one to many settings. Thus they struggle to explicitly correlate pose context with the matching feature frequency bands of query points. As a result, these methods either yield overly smoothed details or introduce noisy artifacts in smooth regions.

In this paper, we investigate new ways of mapping the skeleton input to frequencies of a dynamic NeRF model to tackle the aforementioned challenges. Specifically, we design a network with a branch that is explicit in the frequency space and build a multi-level representation that adapts to pose dependencies. To accomplish this, we utilize Sine functions as activations, leveraging its explicit notion of frequency and its capability to directly enforce high-frequency feature transformations (Sitzmann et al. 2020; Mehta et al. 2021; Wu, Jin, and Moo Yi 2023). The main challenge that we address in this paper is on how to control the frequency of the Sine activation for deforming characters.

We first apply a graph neural network (GNN) (Su, Bagaut-

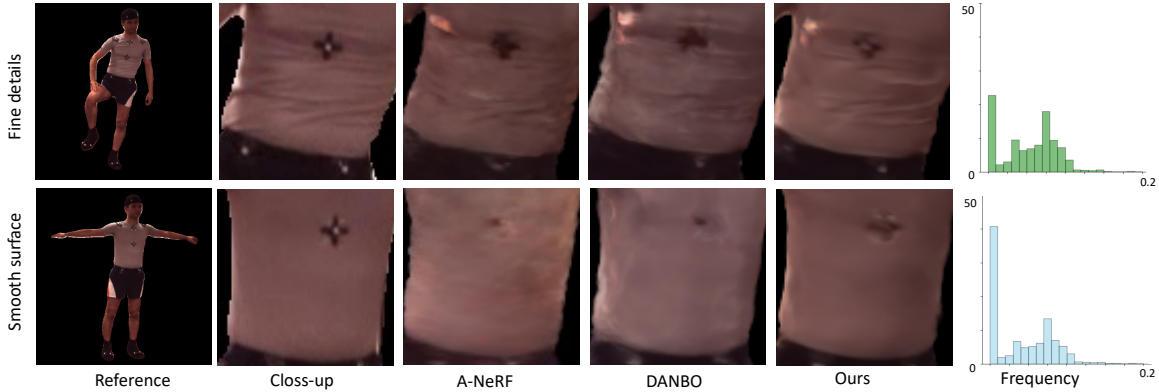


Figure 1: **Motivation.** Our frequency modulation approach enables pose-dependent detail by using explicit frequencies that depend on the pose context, varying over frames and across subjects. Our mapping mitigates artifacts in smooth regions as well as synthesizes fine geometric details faithfully, e.g., when wrinkles are present (1st row). By contrast, existing surface-free representations struggle either with fine details (e.g. marker) or introduce noise artifacts in uniform regions (e.g. the black clouds, 2nd row). To quantify the difference in frequency of these cases, we calculate the standard deviation (STD) pixels within 5×5 patches of the input image and illustrate the frequency histogram of the reference. Even for the same subject in similar pose the frequency distributions are distinct, motivating our pose-dependent frequency formulation.

dinov, and Rhodin 2022) on the input pose to extract correlations between skeleton joints, thereby encoding pose context. Given query point coordinates for NeRF rendering, the joint-specific correlation features are first combined with a part-level feature aggregation function and then utilized to generate point-dependent frequency transformation coefficients. The frequency modulation process takes place within a set of intermediate latent features, allowing us to optimize the modulation effects at different scales effectively. Lastly, similar to existing NeRF methods, we output density and color to synthesize and render images. Across various scenarios, we consistently outperform state-of-the-art methods. Our core contributions are

- We introduce a novel and efficient neural network design with two branches, tailored to generate high-fidelity functional neural representations of human videos through frequency modulation.
- A simple part feature aggregation function that enables high-frequency detail synthesis in sharp regions and reduces artifacts near overlapping joints.
- We conduct thorough evaluation and ablation studies, which delve into the importance of window functions and frequency modulations with state-of-the-art results.

Related Work

Our work is in line with those that apply neural fields to model human avatar representations. Here we survey relevant approaches on neural field (Xie et al. 2022) and discuss the most related neural avatar modeling approaches.

Neural Fields. As a successful application, a breakthrough was brought by Neural Radiance Fields (NeRF) (Mildenhall et al. 2020). Recently, extending NeRF to dynamic scenes becomes more and more popular and enables numerous downstream applications (Park et al. 2021a; Pumarola

et al. 2021; Park et al. 2021b; Cao and Johnson 2023). The key idea is to either extend NeRF with an additional time dimension (T-NeRF) and additional latent code (Gao et al. 2021; Li et al. 2022b, 2021b), or to employ individual multi-layer perceptrons (MLPs) to represent a time-varying deformation field and a static canonical field that represents shape details (Du et al. 2021; Park et al. 2021a,b; Tretschk et al. 2021; Yuan et al. 2021). However, these general extensions from static to dynamic scenes only apply to small deformations and do not generalize to generating humans with novel input poses.

Our method is also related to applying periodic functions for high frequency detail modeling within the context of neural fields. NeRF (Mildenhall et al. 2020) encodes the 3D positions into a high-dimensional latent space using a sequence of fixed periodic functions. Later on, Tancik et al. (Tancik et al. 2020) carefully learn the frequency coefficients of these periodic functions, but they are still shared for the entire scene. In parallel, Sitzmann et al. (Sitzmann et al. 2020) directly uses a Sine-function as the activation function for latent features, which makes frequency bands adaptive to the input. (Lindell et al. 2022; Fathony et al. 2021) further incorporate the multi-scale strategy of spectral domains to further advance the modeling of band-limited signals. Recently, (Hertz et al. 2021; Mehta et al. 2021; Wu, Jin, and Moo Yi 2023) propose to modulate frequency features based on spatial patterns for better detail reconstructions. However, differing from these methods, we explicitly associate the desired frequency transformation coefficients with pose context, tailored to the dynamics in human avatar modeling.

Neural Fields for Avatar Modeling. Using neural networks to model human avatars (Loper et al. 2015) is a widely explored problem (Deng et al. 2020; Saito et al. 2021; Chen et al. 2021). However, learning personalized body models given only videos of a single avatar is particularly challeng-

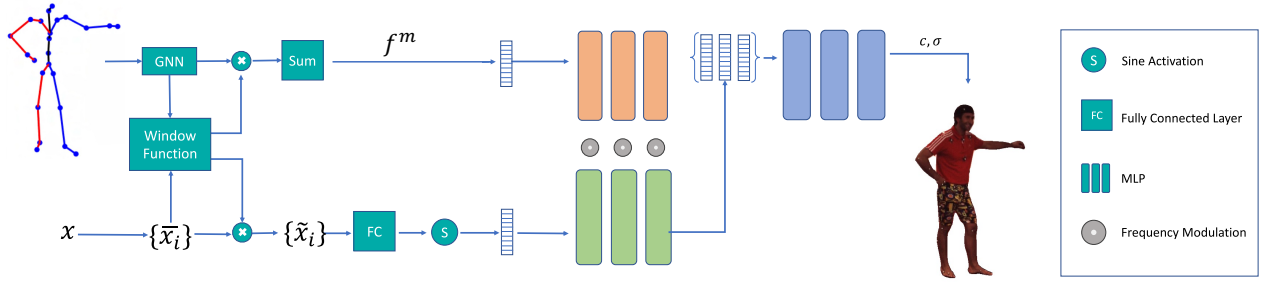


Figure 2: **Method overview.** First, a graph neural network takes a skeleton pose as input to encode correlations of joints. Together with the relative coordinates $\{\tilde{x}_i\}$ of query point x , a window function is learned to aggregate the features from all parts. Then the aggregated GNN features are used to compute frequency coefficients (orange) which later modulate the feature transformation of point x (green). Finally, density σ and appearance c is predicted as in NeRF.

ing which is our research scope in this paper.

In the pursuit of textured avatar modeling, the parametric SMPL body model is a common basis. For instance, (Zheng et al. 2022, 2023) propose partitioning avatar representations into local radiance fields attached to sampled SMPL nodes and learning the mapping from SMPL pose vectors to varying details of human appearance. On the other hand, approaches without a surface prior, such as A-NeRF (Su et al. 2021) and NARF (Noguchi et al. 2021), directly transform the input query points into relative coordinates of skeletal joints. Later on, TAVA (Li et al. 2022a) jointly models non-rigid warping fields and shading effects conditioned on pose vectors. ARAH (Wang et al. 2022) explores ray intersection on a NeRF body model initialized using a pre-trained hypernetwork. DANBO (Su, Bagautdinov, and Rhodin 2022) applies a graph neural network to extract part features and decompose an independent part feature space for a scalable and customizable model. To reconstruct high-frequency details, Neural Actor (Liu et al. 2021) utilizes an image-to-image translation network to learn texture mapping, with a constraint on performers wearing tight clothes for topological consistency. Further studies (Peng et al. 2021b,a; Dong et al. 2022) suggest assigning a global latent code for each training frame to compensate for dynamic appearance. Most recently, HumanNeRF (Weng et al. 2022) and its following works like Vid2Avatar (Guo et al. 2023) and MonoHuman (Yu et al. 2023) show high-fidelity avatar representations for realistic inverse rendering from a monocular video. Despite the significant progress, none of them explicitly associate the pose context with frequency modeling, which we show is crucial for increasing shape and texture detail.

Method

Our objective is to reconstruct a 3D animatable avatar by leveraging a collection of N images, along with the corresponding body pose represented as the sequence of joint angles $[\theta_k]_{k=1}^N$. Our key technical ingredient is a pose-guided frequency modulation network and its integration for avatar reconstruction. Fig. 2 provides a method overview with three main components. First, we employ a Graph Neural Network (GNN) to estimate local relationships between different body parts. The GNN facilitates effective feature aggrega-

tion across body parts, enabling to learn the nearby pose contexts without relying on surface priors. Then the aggregated GNN features are learned to modulate the frequencies of input positions. Lastly, the resulting per-query feature vector is mapped to the corresponding density and radiance at that location as in the original NeRF framework.

Model Poses via Graph Neural Networks

Inspired by DANBO (Su, Bagautdinov, and Rhodin 2022), we adopt a graph representation for the human skeleton, where each node corresponds to a joint that is linked to neighboring joints by bones. For a given pose with N_B joints $\theta = [\omega_1, \omega_2, \dots, \omega_{N_B}]$, where $\omega_i \in \mathbb{R}^6$ (Zhou et al. 2019) is the rotation parameter of bone $i \in \{1, 2, \dots, N_B\}$, we regress a feature vector for each bone part as:

$$[G_1, G_2, \dots, G_{N_B}] = \text{GNN}(\theta), \quad (1)$$

where GNN represents a learnable graph neural network. To process the irregular human skeleton, we employ two graph convolutional layers, followed by per-node 2-layer Multi-Layer Perceptrons (MLPs). To account for the irregular nature of human skeleton nodes, we learn individual MLP weights for each node. Please refer to (Su, Bagautdinov, and Rhodin 2022) for more comprehensive details. Different to DANBO, we do not use these features directly but employ them to drive the frequency modulation adaptively.

Frequency Modulation with GNN Features

Given a query location $x \in \mathbb{R}^3$ in global coordinates, we first map it to the i -th bone-relative space as

$$\begin{bmatrix} \hat{x}_i \\ 1 \end{bmatrix} = T(\omega_i) \begin{bmatrix} x \\ 1 \end{bmatrix}, \quad (2)$$

where $T(\omega_i)$ denotes the world-to-bone coordinates transformation matrix computed by the rotation parameter ω_i . Like DANBO, we first perform a validness test for the scaled relative positions $\{\tilde{x}_i = s_i \cdot \hat{x}_i\}$, where s_i is a learnable scaling factor to control the size of the volume the i -th part contributes to. This facilitates the processing efficiency and concentrates the network on local patterns. Specifically, if no $\{\tilde{x}_i\}$ falls in $[-1, 1]$, x is estimated to locate far from the body surface and is discarded.

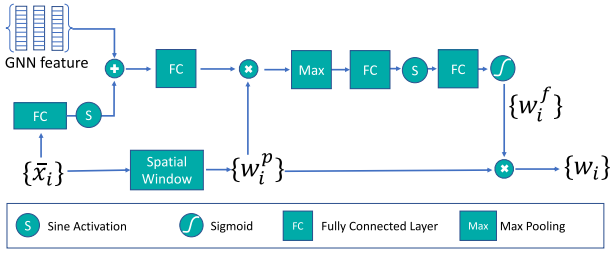


Figure 3: **Learned window function.** The query point location is processed with a spatial and pose-dependent window to remove spurious correlations between distant joints.

Two-stage Window Function. To decide which per-part point-wise features to pass on to the downstream network and address the feature aggregation issues (Su, Bagautdinov, and Rhodin 2022), we design a learnable two-stage window function. As sketched in Fig. 3, the window function takes the per-part GNN feature set $\{G_i\}$ and the scaled relative position set $\{\tilde{x}_i\}$ of a valid point x as inputs. To facilitate learning volume dimensions $\{s_i\}$ that adapt to the body shape and to mitigate seam artifacts, we define

$$w_i^p = \exp(-\alpha(\|\tilde{x}_i\|_2^\beta)), \quad (3)$$

where $\|\cdot\|_2$ is the L_2 -norm. The w_i^p function attenuates the extracted feature based on the relative spatial distances to the bone centers such that multiple volumes are separated via the spatial similarities between x and the given parts. Thus we name w_i^p as the spatial window function. We set $\alpha = 2$ and $\beta = 6$ as in (Lombardi et al. 2021). However, it is possible that one part might prioritize over other parts when multiple valid parts' feature space overlap. This motivates us to take the pose context into account and consider the point-wise feature of each part as the second stage. First, we perform $\hat{x}_i = \sin(\mathbf{W}_c \cdot \tilde{x}_i)$ for each \tilde{x}_i , where \mathbf{W}_c indicates a Gaussian initialized fully-connected layer as in FFN (Tancik et al. 2020). After concatenating $\{\hat{x}_i\}$ and the GNN features $\{G_i\}$ correspondingly, we apply a full-connected layer to regress $\{f_i^p\}$ as the point-wise feature of the i -th part. Then we attenuate the feature as $f_i^w = f_i^p \cdot w_i^p$ to focus on spatially nearby parts.

To further decide which part x belongs to, we compute relative weights by aggregating all $\{f_i^w\}$ through a max pooling for the holistic shape-level representation. The max-pooled feature is fed into a sequence of fully-connected layers which are activated by a Sigmoid function to output a per-part weight w_i^f . We call the feature window function w_i^f to echo the spatial window function w_i^p since it operates on pose features. Finally, we compute the per-part weight $w_i = w_i^p \cdot w_i^f$ and output modulation frequencies as

$$f^m = \sum_{i=0}^{N_B} w_i \cdot G_i, \quad [\theta_1, \theta_2, \dots, \theta_n] = \text{MLP}(f^m), \quad (4)$$

where f^m , θ_i and n represent the aggregated part feature, the modulation frequency coefficient at i -th layer and the layer number of the subsequent modulation module, respectively.

After the two-stage window function, the extracted f^m sparsely correspond to a small part set. To echo the locality assumption throughout the entire network, we also perform the window function w_i for the N_B relative positions of query point x as $\{\tilde{x}_i = \tilde{x}_i \cdot w_i\}$. Note that, we aggregate the part features before MLP-based frequency modulation to avoid time-consuming processing over all parts for all samples. Thus computation complexity reduces significantly.

Frequency Prediction. Inspired by pi-GAN (Chan et al. 2021), we build the backbone network for each x with a series of Sine-activated fully-connected layers (Sitzmann et al. 2020). To this end, we first concatenate all the re-weighted positions $\{\tilde{x}_i\}$ as a whole and input it into a Sine-activated fully-connected layer (Sitzmann et al. 2020). Later on, each fully-connected layer is defined as

$$\mathbf{f}_i = \sin(\theta_i \cdot \mathbf{W}_i \mathbf{f}_{i-1} + \mathbf{b}_i), \quad (5)$$

where \mathbf{W}_i and \mathbf{b}_i are trainable weight and bias in the i -th layer L_i . Finally, we concatenate the Sine-activated features $\{\mathbf{f}_i\}$ as $S(x) = [\mathbf{f}_1, \mathbf{f}_2, \dots, \mathbf{f}_n]$ for further processing.

Design Discussions. Both our method and DANBO (Su, Bagautdinov, and Rhodin 2022) use the GNN features as a building block to measure bone correlations. By contrast to DANBO, we leverage these aggregated GNN features to estimate the appropriate frequencies, driving the frequency modulation for the input positions. This enables the linked MLP networks to adaptively capture a wide spectrum of coarse and fine details with high variability. Moreover, although some work (Hertz et al. 2021; Wu, Jin, and Moo Yi 2023) aims to modulate frequency features with locality, we make the first step for pose-dependent frequency modulation, which is critical in human avatar modeling. We start from existing conceptual components, analyze their limitations, and propose a novel solution. Specifically, we focus on how to connect GNN pose embeddings with frequency transformations. We then propose a simple window function to improve efficiency without losing accuracy which is also special and helpful in neural avatar modeling.

Volume Rendering and Loss Functions

The output feature $S(x)$ can accurately capture the information of pose dependency and spatial positions, and thus enables adaptive pattern synthesis. To obtain high-quality human body, we learn a neural field F to predict the color c and density σ at position x as

$$(c, \sigma) = F(S(x), r), \quad (6)$$

where $r \in \mathbb{R}^2$ indicates the given ray directions. Following the existing neural radiance rendering pipelines for human avatars (Su et al. 2021; Su, Bagautdinov, and Rhodin 2022; Wang et al. 2022), we output the image of the human subject as in the original NeRF:

$$\hat{C}(r) = \sum_{i=1}^n \mathcal{T}_i (1 - \exp(-\sigma_i \delta_i)) \mathbf{c}_i, \quad \mathcal{T}_i = \exp(-\sum_{j=1}^{i-1} \sigma_j \delta_j). \quad (7)$$

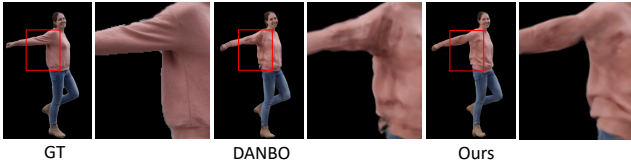


Figure 4: **Unseen pose synthesis on MonoPerfCap.** Compared to DANBO, we can preserve better shape contours and produce realistic cloth wrinkles without artifacts.

Table 1: **Novel-view and novel-pose synthesis results, averaged over the Human3.6M test set.** Our method benefits from the explicit frequency modulations, yielding better perceptual quality, reaching the best overall score in all metrics.

| | Novel view | | | Novel pose | | |
|----------------------------------|-----------------|-----------------|--------------------|-----------------|-----------------|--------------------|
| | PSNR \uparrow | SSIM \uparrow | LPIPS \downarrow | PSNR \uparrow | SSIM \uparrow | LPIPS \downarrow |
| Template/Scan-based prior | | | | | | |
| NeuralBody | 23.36 | 0.905 | 0.140 | 22.81 | 0.888 | 0.157 |
| Anim-NeRF | 23.34 | 0.897 | 0.157 | 22.61 | 0.881 | 0.170 |
| ARAH \dagger | 24.63 | 0.920 | 0.115 | 23.27 | 0.897 | 0.134 |
| Template-free | | | | | | |
| A-NeRF | 24.26 | 0.911 | 0.129 | 23.02 | 0.883 | 0.171 |
| DANBO | 24.69 | 0.917 | 0.116 | 23.74 | 0.901 | 0.131 |
| TAVA | 24.72 | 0.919 | 0.124 | 23.52 | 0.899 | 0.141 |
| Ours | 25.06 | 0.921 | 0.110 | 24.15 | 0.906 | 0.124 |

\dagger : using public release that differs to (Wang et al. 2022).

Here, \hat{C} and δ_i indicate the synthesized image and the distance between adjacent samples along a given ray respectively. Finally, we compute the L_1 loss $\|\cdot\|_1$ for training as

$$\mathcal{L}_{rec} = \sum_{r \in \mathfrak{R}} \left\| \hat{C}(r) - C_{gt}(r) \right\|_1, \quad (8)$$

where \mathfrak{R} is the whole ray set and C_{gt} is the ground truth. The usage of L_1 loss is to enable more robust network training. Following (Lombardi et al. 2021), we add a regularization loss on the scaling factors to prevent the per-bone volumes from growing too large and taking over other volumes:

$$\mathcal{L}_s = \sum_{i=1}^{N_B} (s_i^x \cdot s_i^y \cdot s_i^z), \quad (9)$$

where $\{s_i^x, s_i^y, s_i^z\}$ are the scaling factors along $\{x, y, z\}$ axes respectively. Hence, our total loss with weight λ_s is

$$\mathcal{L} = \mathcal{L}_{rec} + \lambda_s \mathcal{L}_s. \quad (10)$$

Results

In this section, we compare our approach with several state-of-the-art methods, including NeuralBody (Peng et al. 2021b), Anim-NeRF (Peng et al. 2021a), A-NeRF (Su et al. 2021), TAVA (Li et al. 2022a), DANBO (Su, Bagautdinov, and Rhodin 2022), and ARAH (Wang et al. 2022). These methods vary in their utilization of surface-free, template-based, or scan-based priors. Additionally, we conduct an ablation study to assess the improvement achieved by each network component. This study also analyzes and discusses the effects of the learnable window function. Source code will be released with the publication.

Experimental Settings

We evaluate our method on widely recognized benchmarks for body modeling. Following the protocol established by Anim-NeRF, we perform comparisons on the seven actors of the Human3.6M dataset (Ionescu, Li, and Sminchisescu 2011; Ionescu et al. 2013; Peng et al. 2021a) using the method described in (Gong et al. 2018) to compute the foreground maps. Like DANBO, we also apply MonoPerfCap (Xu et al. 2018) as a high-resolution dataset to evaluate the robustness to unseen poses. More details are presented in the appendix.

To ensure a fair comparison, we follow the previous experimental settings including the dataset split and used metrics (Su et al. 2021; Su, Bagautdinov, and Rhodin 2022; Li et al. 2022a). Specifically, we utilize standard image metrics such as pixel-wise Peak Signal-to-Noise Ratio (PSNR) and Structural Similarity Index Metric (SSIM) (Wang et al. 2004) to evaluate the quality of output images. Additionally, we employ perceptual metrics like the Learned Perceptual Image Patch Similarity (LPIPS) (Zhang et al. 2018) to assess the structural accuracy and textured details of the generated images. Since our primary focus is on the foreground subjects rather than the background image, we report the scores based on tight bounding boxes, ensuring the evaluation to be focused on the relevant regions of interest.

Novel View Synthesis

To evaluate the generalization capability under different camera views, we utilize multi-view datasets where the body model is learned from a subset of cameras. The remaining cameras are then utilized as the test set, allowing us to render the same pose from unseen view directions.

We present the visual results in Fig. 5. Comparing to the selected baselines, our method shows superior performance in recovering fine-grained details, as evident in the examples such as the stripe texture depicted on the first row. We attribute this to the explicit frequency modulation which mitigates grainy artifacts and overly smooth regions. Tab. 1 quantifies our method’s empirical advantages, supporting our previous findings.

Novel Pose Rendering

We follow prior work and measure the quality of novel pose synthesis by training on the first part of a video and testing on the remaining frames. Only the corresponding 3D pose is used as input. This tests the generalization of the learned pose modulation strategy and applicability to animation.

We present the visual comparisons for the Human3.6M dataset in Fig. 5, where our method demonstrates superior results than baselines in terms of fine-grained and consistent renderings. Specifically, our method generates sharper details such as those seen in wrinkles and better texture consistency, as exemplified by the clearer marker (highlighted by gray arrow) on 2nd row. Tab. 1 further quantitatively verifies that our method generalizes well to both held-out poses and out-of-distribution poses across the entire test set.

Moreover, we provide the visual comparisons in Fig. 4 and the quantitative metrics in Tab. 2 for the high-resolution

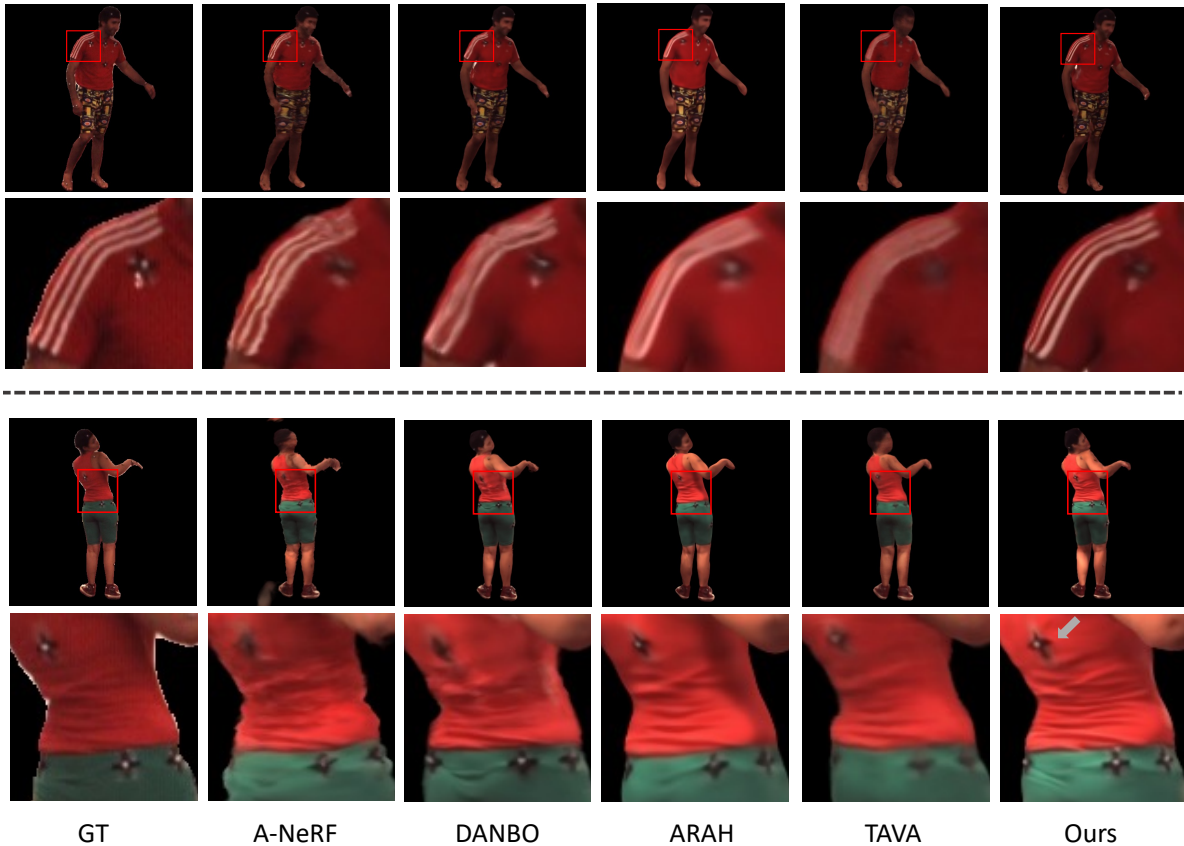


Figure 5: **Visual comparisons for novel view synthesis (1st row) and novel pose rendering (2nd row).** Compared to baselines, we can vividly reproduce the structured patterns (e.g. the stripe on 1st row) and the high-frequency details (e.g. the dynamic wrinkles and highlighted marker textures on 2nd row). Note that it can not be expected that the ground truth is matched perfectly for the novel pose frames that are unseen during training as cloth wrinkles form dynamically.

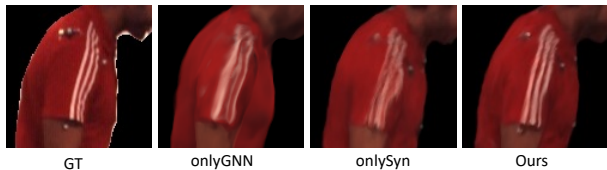


Figure 6: **Ablation study on sub-branch networks.**

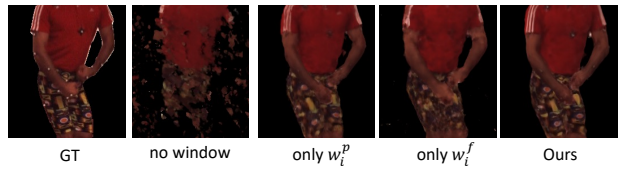


Figure 7: **Ablation study on window functions.**

outdoor monocular video sequences MonoPerfCap (Xu et al. 2018). Being consistent with the results on the Human3.6M sequences, our method presents better capability in learning a generalized model from monocular videos.

Furthermore, we test the animation ability of our approach by driving models learned from the Human3.6M dataset with extreme out-of-distribution poses from AIST (Li et al. 2021a). The qualitative results shown in Fig. 9 validate that even under extreme pose variation our approach produces plausible body shapes with desired texture details while the baseline show severe artifacts. Here no quantitative evaluations are performed since no ground truth data is available.

Geometry Visualization

In Fig. 8, we analyze the geometry reconstructed with our approach against reconstructions from the baseline. Our method captures better body shapes and per-part geometry. Specifically, our results present overall more complete body outline and a smoother surface. In contrast, the baselines predict more noisy blobs near the body surface. Together with the results of novel view and novel pose synthesis, we also attribute our more consistent rendering results across novel views than the baselines to better geometry preservation. This might suggest that more faithful modeling of geometry is also beneficial for the visual fidelity as shown in the appended video.

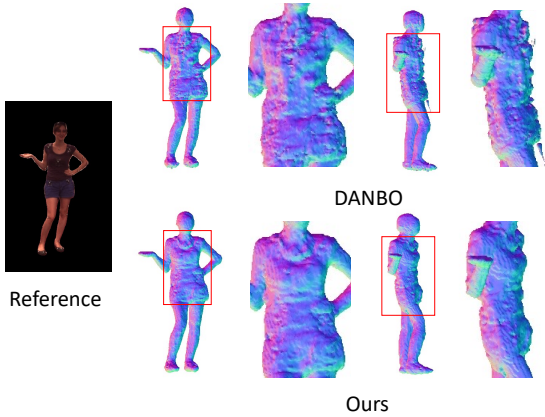


Figure 8: **Geometry reconstruction.** Our method yields more precise, less noisy shape estimates. Some noise remains as no template mesh or other surface prior is used.

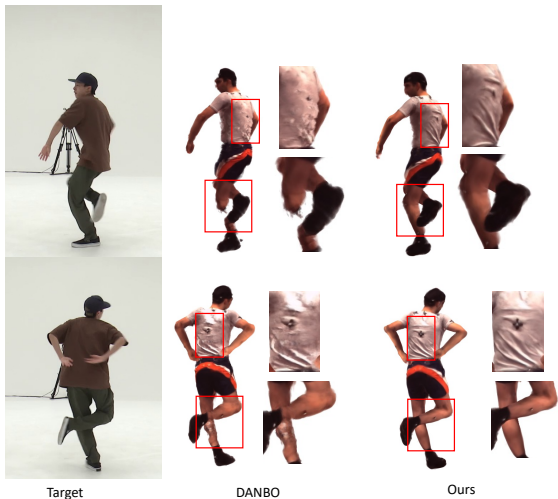


Figure 9: **Animation capability.** Our method maintains the reconstructed high frequency details when retargeting and creates fewer artifacts, lending itself for retargeting.

Ablation Study Results

To test the significance of each component, we conduct the ablation study on Human3.6M S9 with five ablated models:

1. Only preserve the upper branch network with GNN features as onlyGNN;
2. Only preserve the bottom branch network for direct signal synthesis without modulation as onlySyn;
3. For the two-stage window function, we only preserve w_i^p to evaluate the effectiveness of the spatial similarities between x and all bone parts as only w_i^p ;
4. Like 3), we only preserve w_i^f to evaluate the importance of max-pooled object-level feature as only w_i^f ;
5. We remove the whole window function as no window.

In Figures 6-7, we present the qualitative ablation study results. Specifically, the onlyGNN model is prone to pro-

duce blurry textures due to its low frequency bias while the onlySyn model introduces noisy artifacts near stripe textures. Only the combination yields their full advantage and successfully synthesizes structured patterns, as shown in Fig. 6. As mentioned in method section, w_i^p and w_i^f cater for the relationships in position space and feature space, respectively. As shown by the results of novel pose rendering (Fig. 7), neither using w_i^p or w_i^f alone suffices to produce the image quality of the full model, demonstrating the necessity of all contributions. In Tab. 3, we list corresponding quantitative results to further support our statement. Tab. 2 presents the quantitative scores from the MonoPerfCap dataset, showcasing the performance of both the onlyGNN and onlySyn models. Similar to the result differences shown in Tab. 3, our full model consistently outperforms these two ablated models, which reveals our full model’s adaptability to diverse in-the-wild scenarios depicted in high-resolution images. With all these results, we conclude that each component clearly contribute to the empirical success of the full model. More ablation studies on the pose-dependent frequency modulation can be found in the appendix.

| | ND | | WP | | Avg | |
|-------------|--------------|--------------|--------------|--------------|--------------|--------------|
| | PSNR↑ | SSIM↑ | PSNR↑ | SSIM↑ | PSNR↑ | SSIM↑ |
| onlyGNN | 20.03 | 0.841 | 22.71 | 0.863 | 21.37 | 0.852 |
| onlySyn | 19.57 | 0.827 | 22.66 | 0.860 | 21.12 | 0.844 |
| DANBO | 20.10 | 0.842 | 22.39 | 0.861 | 21.25 | 0.852 |
| Ours | 20.55 | 0.853 | 22.85 | 0.866 | 21.70 | 0.860 |

Table 2: **Unseen pose synthesis on MonoPerfCap (Xu et al. 2018).** Our full model shows better overall perceptual quality over chosen models from monocular videos.

| | onlyGNN | onlySyn | only w_i^p | only w_i^f | no window | Ours (full) |
|-------------------|---------|---------|--------------|--------------|-----------|--------------|
| Novel view | | | | | | |
| PSNR↑ | 25.91 | 25.86 | 26.21 | 25.91 | 22.21 | 26.39 |
| SSIM↑ | 0.917 | 0.916 | 0.925 | 0.921 | 0.639 | 0.929 |
| LPIPS↓ | 0.120 | 0.118 | 0.112 | 0.124 | 0.478 | 0.100 |
| Novel pose | | | | | | |
| PSNR↑ | 24.75 | 24.82 | 25.01 | 24.72 | 20.98 | 25.12 |
| SSIM↑ | 0.891 | 0.901 | 0.904 | 0.900 | 0.628 | 0.908 |
| LPIPS↓ | 0.146 | 0.141 | 0.133 | 0.148 | 0.502 | 0.122 |

duce blurry textures due to its low frequency bias while the onlySyn model introduces noisy artifacts near stripe textures. Only the combination yields their full advantage and successfully synthesizes structured patterns, as shown in Fig. 6. As mentioned in method section, w_i^p and w_i^f cater for the relationships in position space and feature space, respectively. As shown by the results of novel pose rendering (Fig. 7), neither using w_i^p or w_i^f alone suffices to produce the image quality of the full model, demonstrating the necessity of all contributions. In Tab. 3, we list corresponding quantitative results to further support our statement. Tab. 2 presents the quantitative scores from the MonoPerfCap dataset, showcasing the performance of both the onlyGNN and onlySyn models. Similar to the result differences shown in Tab. 3, our full model consistently outperforms these two ablated models, which reveals our full model’s adaptability to diverse in-the-wild scenarios depicted in high-resolution images. With all these results, we conclude that each component clearly contribute to the empirical success of the full model. More ablation studies on the pose-dependent frequency modulation can be found in the appendix.

Conclusion

We introduce a novel, frequency-based framework based on NeRF (Mildenhall et al. 2020) that enables the accurate learning of human body representations from videos. The main contribution of our approach is the explicit integration of desired frequency modeling with pose context. When compared to state-of-the-art algorithms, our method demonstrates improved synthesis quality and enhanced generalization capabilities, particularly when faced with unseen poses and camera views.

References

- Agarap, A. F. 2018. Deep learning using rectified linear units (relu). *CoRR*.
- Bagautdinov, T.; Wu, C.; Simon, T.; Prada, F.; Shiratori, T.; Wei, S.-E.; Xu, W.; Sheikh, Y.; and Saragih, J. 2021. Driving-signal aware full-body avatars. *ACM TOG*.
- Cao, A.; and Johnson, J. 2023. Hexplane: A fast representation for dynamic scenes. In *CVPR*.
- Chan, E. R.; Monteiro, M.; Kellnhofer, P.; Wu, J.; and Wetzstein, G. 2021. pi-gan: Periodic implicit generative adversarial networks for 3d-aware image synthesis. In *CVPR*.
- Chen, L.-C.; Papandreou, G.; Schroff, F.; and Adam, H. 2017. Rethinking atrous convolution for semantic image segmentation.
- Chen, X.; Zheng, Y.; Black, M. J.; Hilliges, O.; and Geiger, A. 2021. Snarf: Differentiable forward skinning for animating non-rigid neural implicit shapes. In *ICCV*.
- Deng, B.; Lewis, J. P.; Jeruzalski, T.; Pons-Moll, G.; Hinton, G.; Norouzi, M.; and Tagliasacchi, A. 2020. Nasa neural articulated shape approximation. In *ECCV*.
- Dong, J.; Fang, Q.; Guo, Y.; Peng, S.; Shuai, Q.; Zhou, X.; and Bao, H. 2022. TotalSelfScan: Learning Full-body Avatars from Self-Portrait Videos of Faces, Hands, and Bodies. In *NeurIPS*.
- Du, Y.; Zhang, Y.; Yu, H.-X.; Tenenbaum, J. B.; and Wu, J. 2021. Neural radiance flow for 4d view synthesis and video processing. In *ICCV*.
- Fathony, R.; Sahu, A. K.; Willmott, D.; and Kolter, J. Z. 2021. Multiplicative Filter Networks. In *ICLR*.
- Gao, C.; Saraf, A.; Kopf, J.; and Huang, J.-B. 2021. Dynamic view synthesis from dynamic monocular video. In *ICCV*.
- Gong, K.; Liang, X.; Li, Y.; Chen, Y.; Yang, M.; and Lin, L. 2018. Instance-level human parsing via part grouping network. In *ECCV*.
- Guo, C.; Jiang, T.; Chen, X.; Song, J.; and Hilliges, O. 2023. Vid2Avatar: 3D Avatar Reconstruction from Videos in the Wild via Self-supervised Scene Decomposition. In *CVPR*.
- Hertz, A.; Perel, O.; Giryes, R.; Sorkine-Hornung, O.; and Cohen-Or, D. 2021. Sape: Spatially-adaptive progressive encoding for neural optimization. *NeurIPS*.
- Hu, H.; Xiao, D.; Rhodin, H.; and Murphy, T. H. 2022. Towards a Visualizable, De-identified Synthetic Biomarker of Human Movement Disorders. *Journal of Parkinson's Disease*.
- Ionescu, C.; Li, F.; and Sminchisescu, C. 2011. Latent structured models for human pose estimation. In *ICCV*.
- Ionescu, C.; Papava, D.; Olaru, V.; and Sminchisescu, C. 2013. Human3.6m: Large scale datasets and predictive methods for 3d human sensing in natural environments. *IEEE TPAMI*.
- Jiang, W.; Yi, K. M.; Samei, G.; Tuzel, O.; and Ranjan, A. 2022. Neuman: Neural human radiance field from a single video. In *ECCV*.
- Kingma, D. P.; and Ba, J. 2014. Adam: A method for stochastic optimization. *ICLR*.
- Kolotouros, N.; Pavlakos, G.; Black, M. J.; and Daniilidis, K. 2019. Learning to reconstruct 3D human pose and shape via model-fitting in the loop. In *ICCV*.
- Kwon, Y.; Kim, D.; Ceylan, D.; and Fuchs, H. 2021. Neural human performer: Learning generalizable radiance fields for human performance rendering. *NeurIPS*.
- Li, R.; Tanke, J.; Vo, M.; Zollhöfer, M.; Gall, J.; Kanazawa, A.; and Lassner, C. 2022a. Tava: Template-free animatable volumetric actors. In *ECCV*.
- Li, R.; Yang, S.; Ross, D. A.; and Kanazawa, A. 2021a. Ai choreographer: Music conditioned 3d dance generation with aist++. In *ICCV*.
- Li, T.; Slavcheva, M.; Zollhoefer, M.; Green, S.; Lassner, C.; Kim, C.; Schmidt, T.; Lovegrove, S.; Goesele, M.; Newcombe, R.; et al. 2022b. Neural 3d video synthesis from multi-view video. In *CVPR*.
- Li, Z.; Niklaus, S.; Snavely, N.; and Wang, O. 2021b. Neural scene flow fields for space-time view synthesis of dynamic scenes. In *CVPR*.
- Li, Z.; Zheng, Z.; Liu, Y.; Zhou, B.; and Liu, Y. 2023. Pose-Vocab: Learning Joint-structured Pose Embeddings for Human Avatar Modeling. In *SIGGRAPH*.
- Lindell, D. B.; Van Veen, D.; Park, J. J.; and Wetzstein, G. 2022. BACON: Band-limited Coordinate Networks for Multiscale Scene Representation. *CVPR*.
- Liu, L.; Habermann, M.; Rudnev, V.; Sarkar, K.; Gu, J.; and Theobalt, C. 2021. Neural actor: Neural free-view synthesis of human actors with pose control. *ACM TOG*.
- Lombardi, S.; Simon, T.; Schwartz, G.; Zollhoefer, M.; Sheikh, Y.; and Saragih, J. 2021. Mixture of volumetric primitives for efficient neural rendering. *ACM TOG*.
- Loper, M.; Mahmood, N.; Romero, J.; Pons-Moll, G.; and Black, M. J. 2015. SMPL: A skinned multi-person linear model. *ACM TOG*.
- Mehta, I.; Gharbi, M.; Barnes, C.; Shechtman, E.; Ramamoorthi, R.; and Chandraker, M. 2021. Modulated Periodic Activations for Generalizable Local Functional Representations. In *ICCV*.
- Mildenhall, B.; Srinivasan, P. P.; Tancik, M.; Barron, J. T.; Ramamoorthi, R.; and Ng, R. 2020. Nerf: Representing scenes as neural radiance fields for view synthesis. *ECCV*.
- Noguchi, A.; Sun, X.; Lin, S.; and Harada, T. 2021. Neural articulated radiance field.
- Park, K.; Sinha, U.; Barron, J. T.; Bouaziz, S.; Goldman, D. B.; Seitz, S. M.; and Martin-Brualla, R. 2021a. Nerfies: Deformable neural radiance fields. In *ICCV*.
- Park, K.; Sinha, U.; Hedman, P.; Barron, J. T.; Bouaziz, S.; Goldman, D. B.; Martin-Brualla, R.; and Seitz, S. M. 2021b. HyperNeRF: A Higher-Dimensional Representation for Topologically Varying Neural Radiance Fields. *ACM TOG*.
- Paszke, A.; Gross, S.; Massa, F.; Lerer, A.; Bradbury, J.; Chanan, G.; Killeen, T.; Lin, Z.; Gimelshein, N.; Antiga, L.;

- et al. 2019. Pytorch: An imperative style, high-performance deep learning library.
- Peng, S.; Dong, J.; Wang, Q.; Zhang, S.; Shuai, Q.; Zhou, X.; and Bao, H. 2021a. Animatable neural radiance fields for modeling dynamic human bodies. In *ICCV*.
- Peng, S.; Zhang, Y.; Xu, Y.; Wang, Q.; Shuai, Q.; Bao, H.; and Zhou, X. 2021b. Neural body: Implicit neural representations with structured latent codes for novel view synthesis of dynamic humans. In *CVPR*.
- Pumarola, A.; Corona, E.; Pons-Moll, G.; and Moreno-Noguer, F. 2021. D-nerf: Neural radiance fields for dynamic scenes. In *CVPR*.
- Saito, S.; Yang, J.; Ma, Q.; and Black, M. J. 2021. SCANimate: Weakly supervised learning of skinned clothed avatar networks. In *CVPR*.
- Sitzmann, V.; Martel, J.; Bergman, A.; Lindell, D.; and Wetzstein, G. 2020. Implicit neural representations with periodic activation functions. *NeurIPS*.
- Su, S.-Y.; Bagautdinov, T.; and Rhodin, H. 2022. Danbo: Disentangled articulated neural body representations via graph neural networks. In *ECCV*.
- Su, S.-Y.; Yu, F.; Zollhöfer, M.; and Rhodin, H. 2021. A-nerf: Articulated neural radiance fields for learning human shape, appearance, and pose. *NeurIPS*.
- Tancik, M.; Srinivasan, P.; Mildenhall, B.; Fridovich-Keil, S.; Raghavan, N.; Singhal, U.; Ramamoorthi, R.; Barron, J.; and Ng, R. 2020. Fourier Features Let Networks Learn High Frequency Functions in Low Dimensional Domains. *NeurIPS*.
- Thies, J.; Zollhöfer, M.; and Nießner, M. 2019. Deferred neural rendering: Image synthesis using neural textures. *ACM TOG*.
- Tretschk, E.; Tewari, A.; Golyanik, V.; Zollhöfer, M.; Lassner, C.; and Theobalt, C. 2021. Non-rigid neural radiance fields: Reconstruction and novel view synthesis of a dynamic scene from monocular video. In *ICCV*.
- Wang, S.; Schwarz, K.; Geiger, A.; and Tang, S. 2022. Arah: Animatable volume rendering of articulated human sdfs. In *ECCV*.
- Wang, Z.; Bovik, A. C.; Sheikh, H. R.; and Simoncelli, E. P. 2004. Image quality assessment: from error visibility to structural similarity. *IEEE TIP*.
- Weng, C.-Y.; Curless, B.; Srinivasan, P. P.; Barron, J. T.; and Kemelmacher-Shlizerman, I. 2022. HumanNeRF: Free-viewpoint Rendering of Moving People from Monocular Video. In *CVPR*.
- Wu, Z.; Jin, Y.; and Moo Yi, K. 2023. Neural Fourier Filter Bank. In *CVPR*.
- Xie, Y.; Takikawa, T.; Saito, S.; Litany, O.; Yan, S.; Khan, N.; Tombari, F.; Tompkin, J.; Sitzmann, V.; and Sridhar, S. 2022. Neural Fields in Visual Computing and Beyond. *Computer Graphics Forum*.
- Xu, W.; Chatterjee, A.; Zollhöfer, M.; Rhodin, H.; Mehta, D.; Seidel, H.-P.; and Theobalt, C. 2018. Monoperfcap: Human performance capture from monocular video. *ACM TOG*.
- Yu, Z.; Cheng, W.; Liu, X.; Wu, W.; and Lin, K.-Y. 2023. MonoHuman: Animatable Human Neural Field from Monocular Video. In *CVPR*.
- Yuan, W.; Lv, Z.; Schmidt, T.; and Lovegrove, S. 2021. Star: Self-supervised tracking and reconstruction of rigid objects in motion with neural rendering. In *CVPR*.
- Zhang, R.; Isola, P.; Efros, A. A.; Shechtman, E.; and Wang, O. 2018. The unreasonable effectiveness of deep features as a perceptual metric. In *CVPR*.
- Zheng, Z.; Huang, H.; Yu, T.; Zhang, H.; Guo, Y.; and Liu, Y. 2022. Structured local radiance fields for human avatar modeling. In *CVPR*.
- Zheng, Z.; Zhao, X.; Zhang, H.; Liu, B.; and Liu, Y. 2023. AvatarRex: Real-time Expressive Full-body Avatars. *ACM TOG*.
- Zhou, Y.; Barnes, C.; Lu, J.; Yang, J.; and Li, H. 2019. On the continuity of rotation representations in neural networks. In *CVPR*.

Pose Modulated Avatars from Video

(Supplementary Material)

In this part, we first present the details about method implementation, used dataset and data split. Then we provide more comparison results on the frequency histograms, geometry visualization and motion retargeting. We also attach more ablation studies to emphasize the significance of pose-guided frequency modulation and window functions. More qualitative results for novel view synthesis and novel pose rendering are provided as well. Finally, we discuss the limitations and social impacts of this project. See the attached video for the animation and geometry visualization results.

Implementation Details

For consistency, we maintain the same hyper-parameter settings across various testing experiments, including the loss function with weight λ_s , the number of training iterations, and the network capacity and learning rate. All the hyper-parameters are chosen depending on the final accuracy on chosen benchmarks. Our method is implemented using PyTorch (Paszke et al. 2019). We utilize the Adam optimizer (Kingma and Ba 2014) with default parameters $\beta_1 = 0.9$ and $\beta_2 = 0.99$. We employ the step decay schedule to adjust the learning rate, where the initial learning rate is set to 5×10^{-4} and we drop the learning rate to 10% every 500000 iterations. Like former methods (Su et al. 2021; Su, Bagautdinov, and Rhodin 2022), we set $\lambda_s = 0.001$ and $N_B = 24$ to accurately capture the topology variations and avoid introducing unnecessary training changes. The learnable parameters in GNN, window function and the frequency modulation part are activated by the Sine function while other parameters in the neural field F are activated by Relu (Agarap 2018). We train our network on a single NVidia RTX 3090 GPU for about 20 hours.

More Details about Datasets

Follow the experimental settings of previous methods (Su et al. 2021; Su, Bagautdinov, and Rhodin 2022), we choose the Human3.6M (Ionescu, Li, and Sminchisescu 2011) and MonoPerfCap (Xu et al. 2018) as the evaluation benchmarks. These datasets cover the indoor and outdoor scenes captured by monocular and multi-view videos. Specifically, we use a total of 7 subjects for evaluation under the same evaluation protocol as in AnimNeRF (Peng et al. 2021a). We compute the foreground images with (Gong et al. 2018) to focus on the target characters. Likewise, we adopt the identical pair of sequences and configuration as employed in A-NeRF (Su et al. 2021): Weipeng and Nadia, consisting of 1151 and 1635 images each, with a resolution of 1080×1920 . We estimate the human and camera poses using SPIN (Kolotouros et al. 2019) and following pose refinement (Su et al. 2021). We apply the released DeepLabv3 model (Chen et al. 2017) to estimate the foreground masks. The data split also stays the same as the aforementioned



Figure A: **Visual comparisons on MonoPerfCap.** Our method can preserve better shape contours without artifacts (highlighted by the red arrow).

methods for a fair comparison.

More Results

Histogram Comparisons. Showing the frequency histograms of different frames, like the Fig. 1 in the main text, appear to be a clear solution to demonstrate our motivation. Thus we provide more examples and corresponding analysis here. Using the two close-ups in Fig. 1 of the main text, we present the corresponding frequency histograms for each method in Fig. B. To test our effectiveness when training over long sequences, we provide the histogram results of two frames collected in the ZJU-MoCap (Peng et al. 2021b) dataset, in Fig. E. Compared to DANBO, our method can produce more similar contours to the ground truth histograms. Additionally, the matched histogram distances (shown below the histogram subfigures and denoted as **F-Dist**) further confirm our advantages of producing adaptive frequency distributions which is the key point of our method.

Besides measuring the holistic histogram similarities, we directly compute a frequency map by regarding the standard deviation (STD) value at each pixel as a gray-scale value. As evidenced in Fig. E, our method provides significantly improved results, as represented by the error images between the output frequencies and the ground truth values. All these results reveal that our method can faithfully reconstruct the desired frequency distributions both locally and holistically.

Comparisons with DANBO. Pose-modulated frequency learning plays a critical role in our method. To demonstrate the importance of this concept, we present more comparisons with DANBO which performs frequency modeling implicitly. In Fig. H and Fig. I, our method is better at preserving large-scale shape contours as well as fine-grained textures with high-frequency details. To show our empirical advantages on high-resolution outdoor scenes, we report the qualitative comparisons on two MonoPerfCap characters in Fig. A. Compared to DANBO, our method preserves more clearer boundaries (e.g. the hand on 1st row) with less artifacts (e.g. the black blob on 2nd row).

Complete Metrics on Human3.6M sequences. Besides the

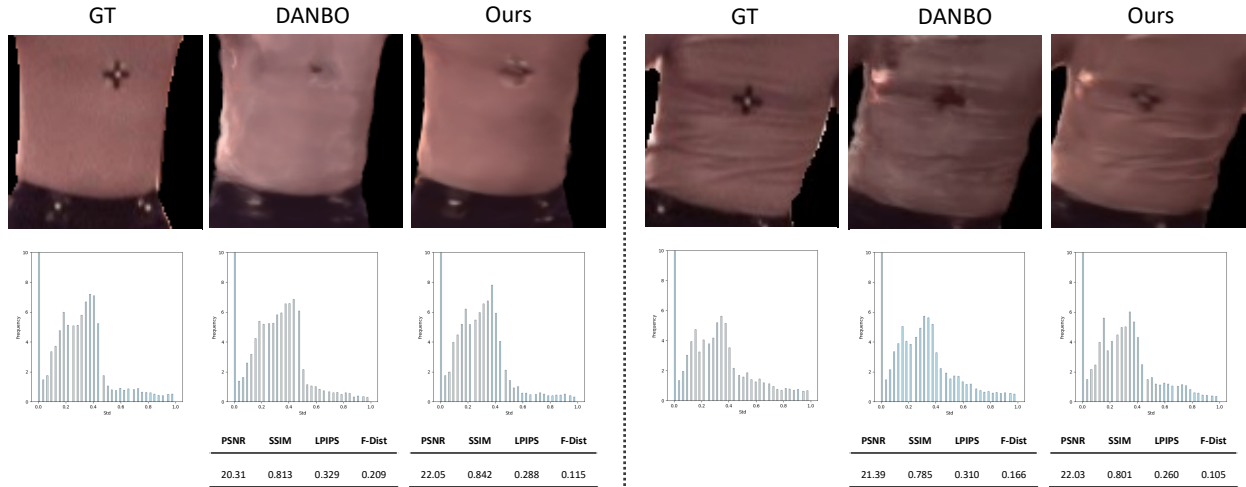


Figure B: **Motivation Demonstration on Human3.6M frames.** Using the two frames in Fig. 1 of the main text, we present the frequency histograms, compute three image quality metrics (e.g. PSNR, SSIM, LPIPS) and the distances between the output frequency map and ground truth values (F-Dist) to justify our pose-guided frequency modulation. Compared to DANBO which modulates frequencies implicitly, our method can synthesize higher-quality images with more adaptive frequency distributions across different pose contexts.

Table A: **Novel-view synthesis results on the Human3.6M (Ionescu, Li, and Sminchisescu 2011) test set.** Our method benefits from the explicit frequency modulations, leading to better perceptual quality. It matches or outperforms all baselines across subjects, reaching the best overall score in all three metrics.

| | S1 | | | S5 | | | S6 | | | S7 | | | S8 | | | S9 | | | S11 | | | Avg | | |
|----------------------------------|-----------------|-----------------|--------------------|--------------|--------------|--------------|--------------|--------------|--------------|--------------|--------------|--------------|-----------------|-----------------|--------------------|--------------|--------------|--------------|--------------|--------------|--------------|--------------|--------------|--------------|
| | PSNR \uparrow | SSIM \uparrow | LPIPS \downarrow | PSNR | SSIM | LPIPS | PSNR | SSIM | LPIPS | PSNR | SSIM | LPIPS | PSNR \uparrow | SSIM \uparrow | LPIPS \downarrow | PSNR | SSIM | LPIPS | PSNR | SSIM | LPIPS | PSNR | SSIM | LPIPS |
| Template/Scan-based prior | | | | | | | | | | | | | | | | | | | | | | | | |
| NeuralBody | 22.88 | 0.897 | 0.139 | 24.61 | 0.917 | 0.128 | 22.83 | 0.888 | 0.155 | 23.17 | 0.915 | 0.132 | 21.72 | 0.894 | 0.151 | 24.29 | 0.911 | 0.122 | 23.70 | 0.896 | 0.168 | 23.36 | 0.905 | 0.140 |
| Anim-NeRF | 22.74 | 0.896 | 0.151 | 23.40 | 0.895 | 0.159 | 22.85 | 0.871 | 0.187 | 21.97 | 0.891 | 0.161 | 22.82 | 0.900 | 0.146 | 24.86 | 0.911 | 0.145 | 24.76 | 0.907 | 0.161 | 23.34 | 0.897 | 0.157 |
| ARAH \dagger | 24.53 | 0.921 | 0.103 | 24.67 | 0.921 | 0.115 | 24.37 | 0.904 | 0.133 | 24.41 | 0.922 | 0.115 | 24.15 | 0.924 | 0.104 | 25.43 | 0.924 | 0.112 | 24.76 | 0.918 | 0.128 | 24.63 | 0.920 | 0.115 |
| Template-free | | | | | | | | | | | | | | | | | | | | | | | | |
| A-NeRF | 23.93 | 0.912 | 0.118 | 24.67 | 0.919 | 0.114 | 23.78 | 0.887 | 0.147 | 24.40 | 0.917 | 0.125 | 22.70 | 0.907 | 0.130 | 25.58 | 0.916 | 0.126 | 24.38 | 0.905 | 0.152 | 24.26 | 0.911 | 0.129 |
| DANBO | 23.95 | 0.915 | 0.107 | 24.85 | 0.923 | 0.107 | 24.54 | 0.903 | 0.129 | 24.45 | 0.920 | 0.113 | 23.36 | 0.917 | 0.116 | 26.15 | 0.925 | 0.108 | 25.58 | 0.917 | 0.127 | 24.69 | 0.917 | 0.116 |
| TAVA | 25.28 | 0.928 | 0.108 | 24.00 | 0.916 | 0.122 | 23.44 | 0.894 | 0.138 | 24.25 | 0.916 | 0.130 | 23.71 | 0.921 | 0.116 | 26.20 | 0.923 | 0.119 | 26.17 | 0.928 | 0.133 | 24.72 | 0.919 | 0.124 |
| Ours | 24.83 | 0.922 | 0.102 | 24.97 | 0.925 | 0.102 | 24.55 | 0.903 | 0.124 | 24.65 | 0.923 | 0.107 | 24.11 | 0.922 | 0.108 | 26.39 | 0.929 | 0.100 | 25.88 | 0.921 | 0.128 | 25.06 | 0.921 | 0.110 |

\dagger : we evaluate using the officially released ARAH, which has undergone refactorization, resulting in slightly different numbers to the ones in (Wang et al. 2022).

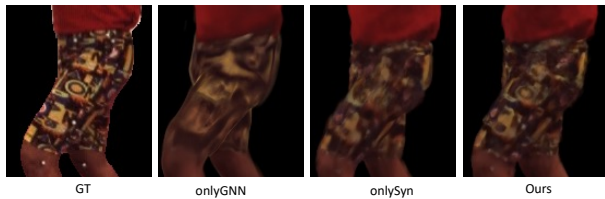


Figure C: Ablation study on sub-branch networks with novel pose rendering.

overall average numbers in the Tab. 1 of the main text, we also report a per-subject breakdown of the quantitative metrics against all baseline methods. Specifically, Tab. A lists the scores for the novel view synthesis while Tab. B details each method's results in novel pose rendering. Being consistent with the visual results shown in Fig. 5 of the main text, our method almost outperforms all baselines for all subjects.

Visual Comparisons with Baselines. Besides the results in



Figure D: Ablation study on window functions with novel view synthesis.

Fig. 5 of the main text, we offer two more characters from Human3.6M sequences to evaluate the results on novel view synthesis and novel pose rendering. As shown in Fig. L, we can successfully reproduce the detailed shape structures (e.g. the hand on 1st row) and high-frequency wrinkles (e.g. 2nd row). These findings stay consistent with the discussions in main text and the quantitative results in Tab. A-B.

Ablation studies. We formulate our framework from connections between frequencies and pose contexts. To more

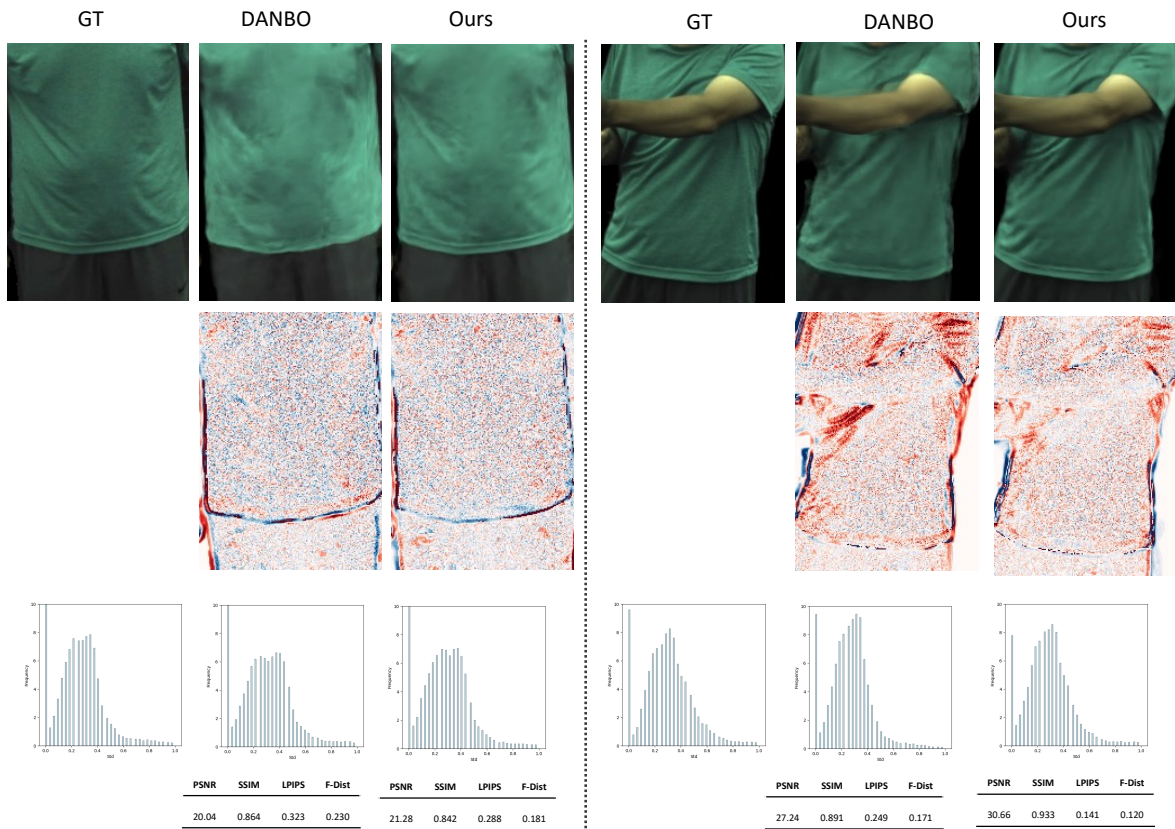


Figure E: **Motivation Demonstration on ZJU-Mocap frames.** To test our effectiveness over long video sequences, we qualitatively and quantitatively evaluate our method with two ZJU-Mocap frames. Being consistent with the findings in Fig. B, our method outperforms DANBO with more similar frequency histograms (3^{rd} row) and better quantitative metrics on image quality and frequency modeling (last row). Additionally, we further illustrate the color-coded frequency error maps (2^{nd} row) for both methods to show that our method can faithfully reconstruct the desired frequency distributions both locally and holistically. For the left frame with smooth patterns, our method introduces slightly few frequency errors as it is easy to model low-frequency variations. On the other hand, for the right frame with much more high-frequency wrinkles, our method faithfully reproduces the desired frequencies with significantly less errors, which clearly demonstrate the importance of our pose-guided frequency modulation. Here red denotes positive and blue denotes negative errors.

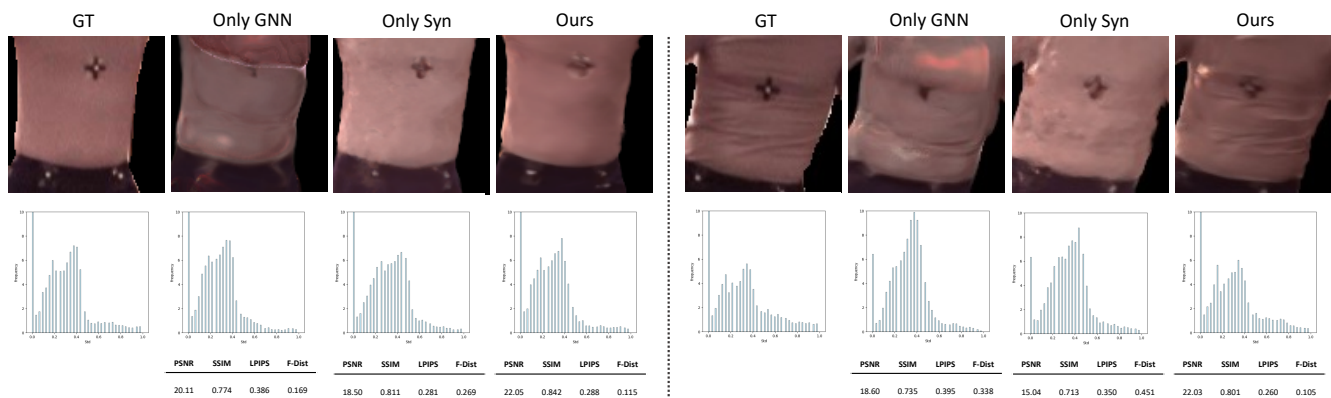


Figure F: **Ablation study on the network components with frequency analysis.** Our full model produces more adaptive frequency distributions and higher image quality than the ablated models.

Table B: Novel pose rendering results on the Human3.6M (Ionescu, Li, and Sminchisescu 2011) test set. Our pose guided frequency modulation pipeline generalizes better across unseen poses.

| | S1 | | | S5 | | | S6 | | | S7 | | | S8 | | | S9 | | | S11 | | | Avg | | |
|----------------------------------|-----------------|-----------------|--------------------|--------------|--------------|--------------|--------------|--------------|--------------|--------------|--------------|--------------|-----------------|-----------------|--------------------|--------------|--------------|--------------|--------------|--------------|--------------|--------------|--------------|--------------|
| | PSNR \uparrow | SSIM \uparrow | LPIPS \downarrow | PSNR | SSIM | LPIPS | PSNR | SSIM | LPIPS | PSNR | SSIM | LPIPS | PSNR \uparrow | SSIM \uparrow | LPIPS \downarrow | PSNR | SSIM | LPIPS | PSNR | SSIM | LPIPS | PSNR | SSIM | LPIPS |
| Template/Scan-based prior | | | | | | | | | | | | | | | | | | | | | | | | |
| NeuralBody | 22.10 | 0.878 | 0.143 | 23.52 | 0.897 | 0.144 | 23.42 | 0.892 | 0.146 | 22.59 | 0.893 | 0.163 | 20.94 | 0.876 | 0.172 | 23.05 | 0.885 | 0.150 | 23.72 | 0.884 | 0.179 | 22.81 | 0.888 | 0.157 |
| Anim-NeRF | 21.37 | 0.868 | 0.167 | 22.29 | 0.875 | 0.171 | 22.59 | 0.884 | 0.159 | 22.22 | 0.878 | 0.183 | 21.78 | 0.882 | 0.162 | 23.73 | 0.886 | 0.157 | 23.92 | 0.889 | 0.176 | 22.61 | 0.881 | 0.170 |
| ARAH [†] | 23.18 | 0.903 | 0.116 | 22.91 | 0.894 | 0.133 | 23.91 | 0.901 | 0.125 | 22.72 | 0.896 | 0.143 | 22.50 | 0.899 | 0.128 | 24.15 | 0.896 | 0.135 | 23.93 | 0.899 | 0.143 | 23.27 | 0.897 | 0.134 |
| Template-free | | | | | | | | | | | | | | | | | | | | | | | | |
| A-NeRF | 22.67 | 0.883 | 0.159 | 22.96 | 0.888 | 0.155 | 22.77 | 0.869 | 0.170 | 22.80 | 0.880 | 0.182 | 21.95 | 0.886 | 0.170 | 24.16 | 0.889 | 0.164 | 23.40 | 0.880 | 0.190 | 23.02 | 0.883 | 0.171 |
| DANBO | 23.03 | 0.895 | 0.121 | 23.66 | 0.903 | 0.124 | 24.57 | 0.906 | 0.118 | 23.08 | 0.897 | 0.139 | 22.60 | 0.904 | 0.132 | 24.79 | 0.904 | 0.130 | 24.57 | 0.901 | 0.146 | 23.74 | 0.901 | 0.131 |
| TAVA | 23.83 | 0.908 | 0.120 | 22.89 | 0.898 | 0.135 | 24.54 | 0.906 | 0.122 | 22.33 | 0.882 | 0.163 | 22.50 | 0.906 | 0.130 | 24.80 | 0.901 | 0.138 | 25.22 | 0.913 | 0.145 | 23.52 | 0.899 | 0.141 |
| Ours | 23.73 | 0.903 | 0.114 | 23.65 | 0.905 | 0.117 | 24.77 | 0.908 | 0.117 | 23.59 | 0.904 | 0.133 | 23.16 | 0.909 | 0.126 | 25.12 | 0.908 | 0.122 | 25.03 | 0.907 | 0.143 | 24.15 | 0.906 | 0.124 |

[†]: we evaluate using the officially released ARAH, which has undergone refactorization, resulting in slightly different numbers to the ones in (Wang et al. 2022).

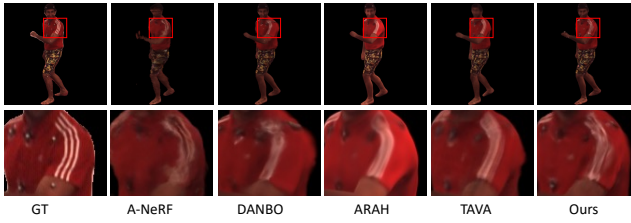


Figure G: **Failure case.** How to generalize to challenging cases is still an open problem, where all methods fail to capture the stripe-wise textures under this pose.



Figure H: **Additional comparison results with DANBO for novel view synthesis.** Due to the adaptive frequency modulation, our method can better synthesize the shape contour (e.g. hands on 1st column), the sharp patterns (e.g. the marker on 2nd column), and high-frequency details (e.g. the wrinkles on 1st column and the pant textures on 3rd column). Otherwise, DANBO which achieves frequency learning implicitly, blurs the sharp patterns and smoothes the fine-grained details.



Figure I: **Additional comparison results with DANBO for novel pose rendering.** Due to the adaptive frequency modulation, our method successfully reduces the noisy artifacts on 1st column, reproduces the white markers on 2nd column and the black marker on 3rd column, reconstructs the sharp shape contours (e.g. the hand) on both 4th and 5th columns. Otherwise, DANBO which achieves frequency learning implicitly, blurs the sharp contours and smoothes the significant patterns with fine-grained details.

comprehensively evaluate the effectiveness of our pose-guided frequency modulation concept, we provide one more visual comparison in Fig. C. It is clear that only our full model successfully synthesizes high frequency patterns, e.g., shown in the pant region.

To additionally showcase the capabilities in reproducing the frequency distributions, we illustrate the frequency histograms for the ground truth images and the network outputs in Fig. F. Our full model remarkably reduces the gap to the ground truth histograms qualitatively and quantitatively.

Moreover, as shown in Fig. J, our full model presents much better time consistency than ablated models. Specifically, the full model constantly preserves more adaptive details (e.g. the patterns in the pant region) than the onlyGNN model and synthesizes more structured stripe-wise patterns than the onlySyn model. Moreover, the onlySyn model distorts the leg shape on the last column.

To highlight the empirical importance of the window function w_i^p and w_i^f , Fig. D depicts qualitative differences between the ablated baselines and our full model. It is clear that using w_i^p or w_i^f alone cannot produce the image quality of the full model, demonstrating the necessity of the window function design.

Geometry Visualization. The attached video visualizes two examples for the geometry reconstruction comparison with DANBO. Like the discussions in the main text, we can

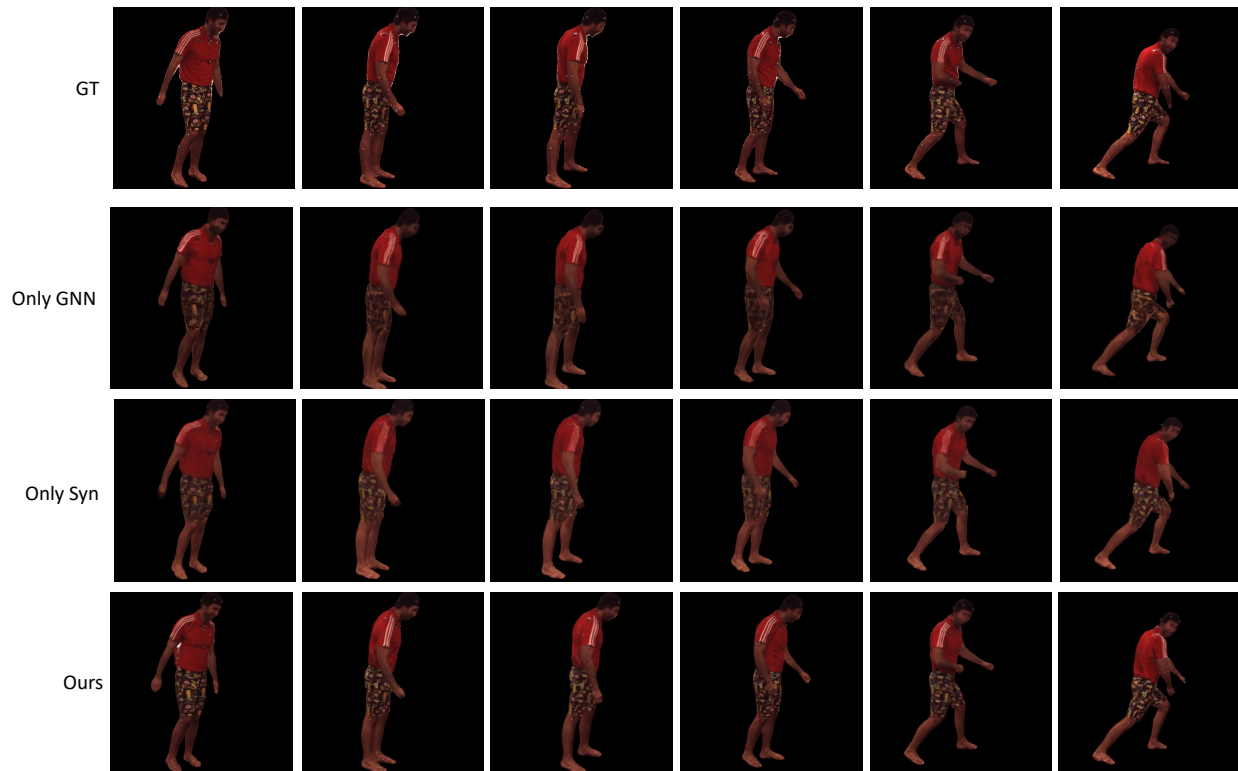


Figure J: **Abaltion study on the network components with time consistency analysis.** Our full model can consistently produce more adaptive details (e.g. in the pant region), synthesize more structured textures (e.g. the stripes) and preserve more realistic contours (e.g. the leg shape). See texts for details.

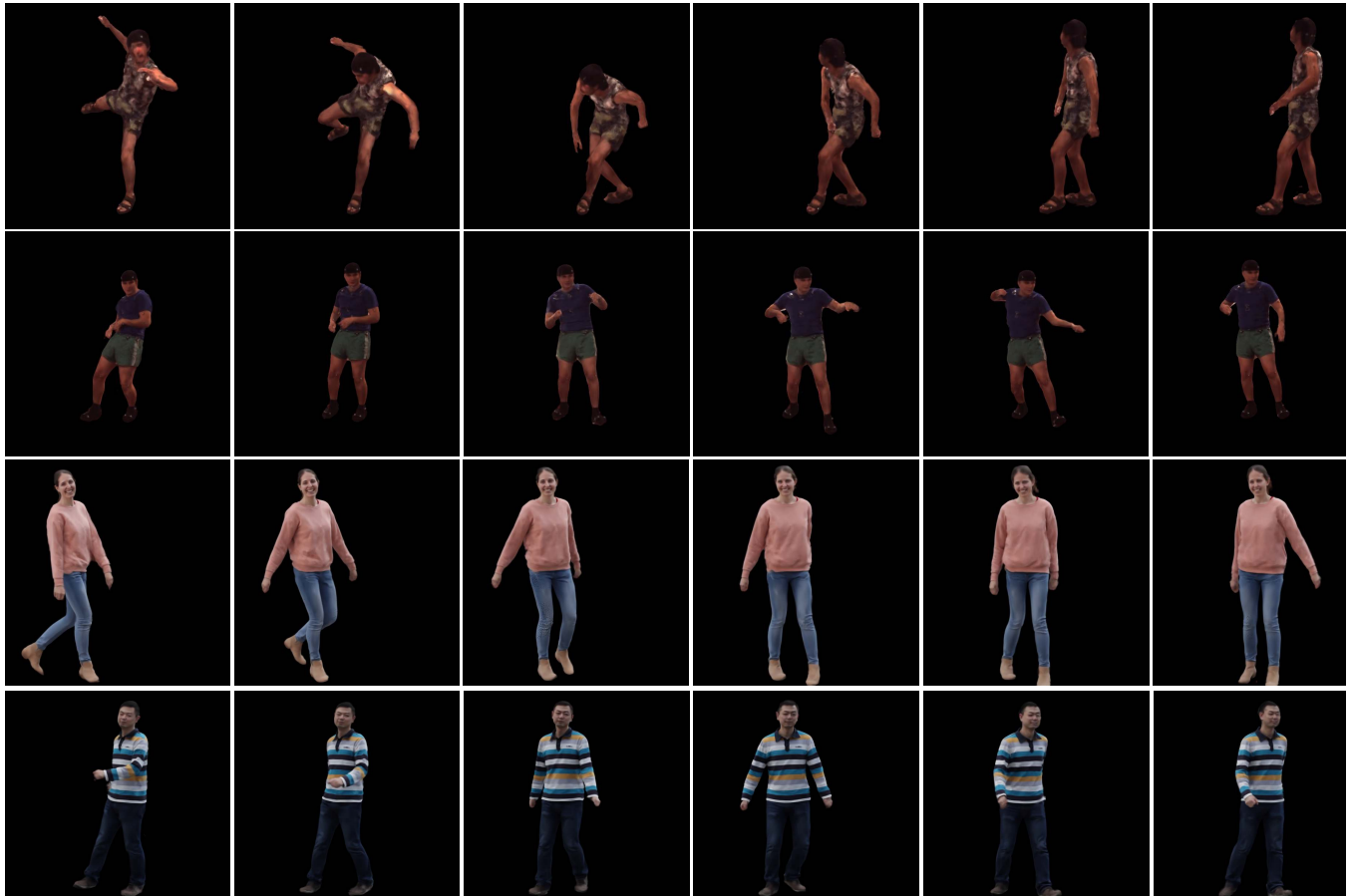


Figure K: **Unseen pose renderings for the sequences** from both Human3.6M (top two rows) and MonoPerfCap (bottom two rows). Our network is robust to various poses across different datasets.

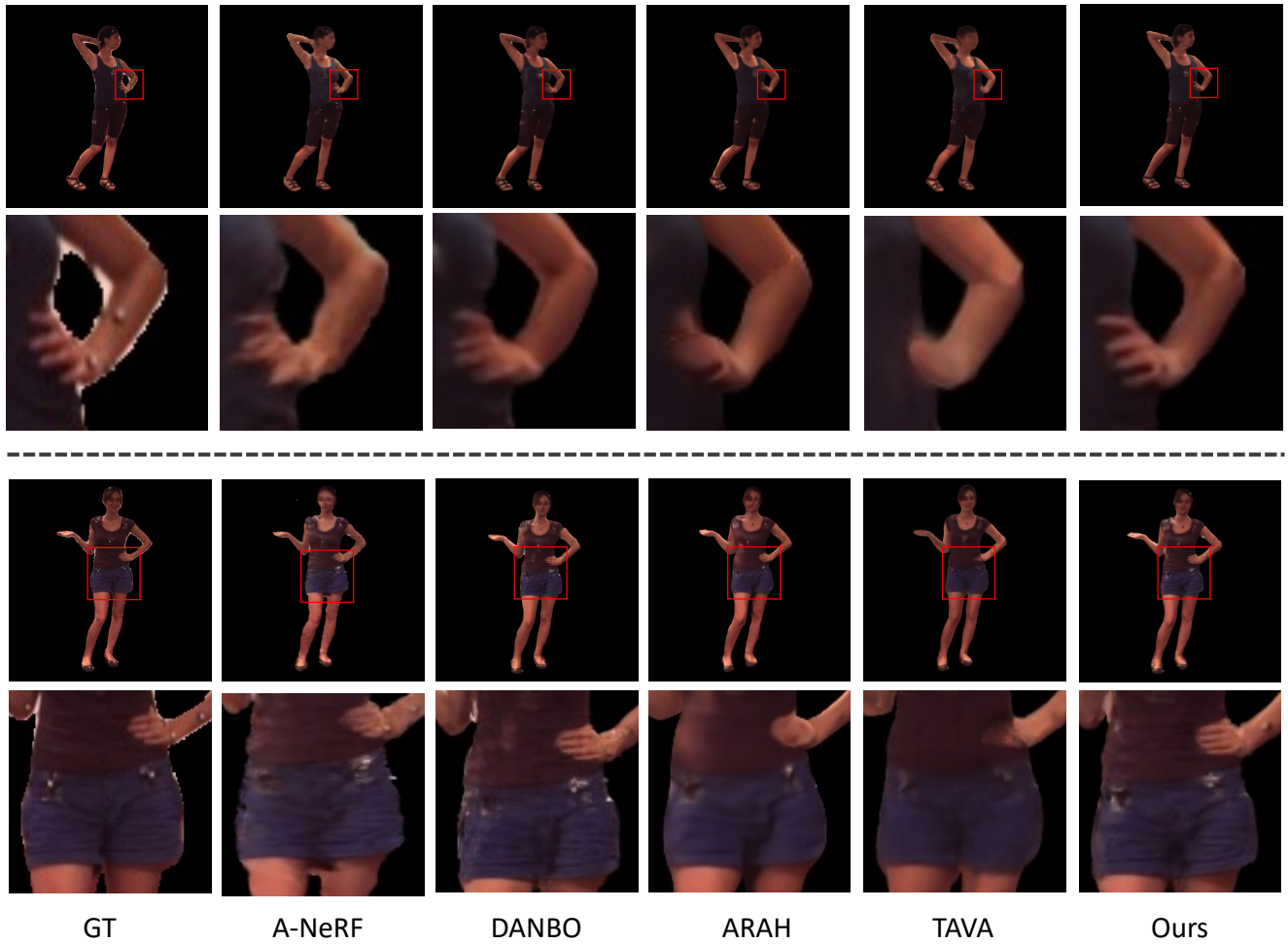


Figure L: **Visual comparisons for novel view synthesis (1st row) and novel pose rendering (2nd row).** Compared to baselines, we can faithfully reconstruct the shape boundaries (e.g. the hands on both 1st and 2nd rows) and the high-frequency details (e.g. the dynamic wrinkles on 2nd row).

present overall more complete body outline and a smoother surface than the baseline. Please see video for details.

Motion Retargeting. Generality to unseen human poses is critical to a number of down-streamed applications, e.g. Virtual Reality. We provide two examples in the attached video. Although our model is trained on the Human3.6M sequences, it can consistently be adapted to the unseen poses with challenging movements. The desired time consistency convincingly demonstrates our strong generality to out-of-the-distribution poses.

More Visual Results. In order to assess the performance of our method in handling unseen camera views and human skeletons, we provide additional results showcasing novel view synthesis in Fig. M and novel pose rendering in Fig. N. We also illustrate the rendering results for different sequences of Human3.6M and MonoPerfCap datasets for unseen poses in Fig. K.

From the results, it is evident that our method, with its developed frequency modulation modeling, effectively captures diverse texture details and shape contours even when confronted with human poses that differ significantly from those in the training set. This empirical advantage can be attributed to the adaptive detail modeling capabilities facilitated by pose-modulated frequency learning.

Limitations and Discussions

Although our method is faster than other neural field approaches, computation time remains a constraint for real-time use. Our method is also person-specific, demanding individual training for each person. And our method heavily relies on accurate camera parameters and lacks support for property editing like pattern transfer. Thus this approach shines with ample training time and available data. Additionally, as shown in Fig. G, under extreme challenges, our method cannot vividly reproduce the desired patterns but introduces blurry artifacts. However, we would like to note that, how to advance the generalization to such cases is still open since the existing methods suffer from similar or worse artefacts as well.

Social Impacts. Our research holds the promise of greatly improving the efficiency of human avatar modeling pipelines, promoting inclusivity for underrepresented individuals and activities in supervised datasets. However, it's imperative to address the ethical aspects and potential risks of creating 3D models without consent. Users must rely on datasets specifically collected for motion capture algorithm development, respecting proper consent and ethical considerations. Furthermore, in the final version, all identifiable faces will be blurred for anonymity.



Figure M: Additional visual results for novel view synthesis. It is clear that our method can faithfully reproduce a larger spectrum of details, from large-scale shape contours (e.g. 1st row) to fine-grained textures (e.g. 2nd row), across different scenes.



Figure N: Additional visual results for novel pose rendering. It is clear that our method can generalize well to the unseen poses with different patterns.